Lawrence Berkeley National Laboratory
LBL Publications

Title
Fermi Level Engineering of Passivation and Electron Transport Materials for p-Type CuBi2O4 Employing a High-Throughput Methodology

Permalink
https://escholarship.org/uc/item/1cp665j9

Journal
Advanced Functional Materials, 30(24)

ISSN
1616-301X

Authors
Zhang, Zemin
Lindley, Sarah A
Guevarra, Dan
et al.

Publication Date
2020-06-01

DOI
10.1002/adfm.202000948

Peer reviewed

eScholarship.org Powered by the California Digital Library
University of California

Fermi Level Engineering of Passivation and Electron Transport Materials for p-Type $CuBi_2O_4$ Employing a High-Throughput Methodology

Zemin Zhang, Sarah A. Lindley, Dan Guevarra, Kevin Kan, Aniketa Shinde, John M. Gregoire, Weihua Han, Erqing Xie, Joel A. Haber, and Jason K. Cooper**

Metal oxide semiconductors are promising for solar photochemistry if the issues of excessive charge carrier recombination and material degradation can be resolved, which are both influenced by surface quality and interface chemistry. Coating the semiconductor with an overlayer to passivate surface states is a common remedial strategy but is less desirable than application of a functional coating that can improve carrier extraction and reduce recombination while mitigating corrosion. In this work, a data-driven materials science approach utilizing high-throughput methodologies, including inkjet printing and scanning droplet electrochemical cell measurements, is used to create and evaluate multi-element coating libraries to discover new classes of candidate passivation and electron-selective contact materials for p-type $CuBi_2O_4$. The optimized overlayer ($Cu_{1.5}TiO_z$) improves the onset potential by 110 mV, the photocurrent by 2.8×, and the absorbed photon-to-current efficiency by 15.5% compared to non-coated photoelectrodes. It is shown that these enhancements are related to reduced surface recombination through passivation of surface defect states as well as improved carrier extraction efficiency through Fermi level engineering. This work presents a generalizable, high-throughput method to design and optimize passivation materials for a variety of semiconductors, providing a powerful platform for development of high-performance photoelectrodes for incorporation into solar-fuel generation systems.

Z. Zhang, S. A. Lindley, J. K. Cooper
Joint Center for Artificial Photosynthesis
Lawrence Berkeley National Laboratory
Berkeley, CA 94720, USA
E-mail: jahaber@caltech.edu

Z. Zhang, W. Han, E. Xie
School of Physical Science and Technology
Lanzhou University
Lanzhou 730000, China

D. Guevarra, K. Kan, A. Shinde, J. M. Gregoire, J. A. Haber
Joint Center for Artificial Photosynthesis
California Institute of Technology
Pasadena, CA 91125, USA
E-mail: jkcooper@lbl.gov

J. K. Cooper
Chemical Sciences Division
Lawrence Berkeley National Laboratory
Berkeley, CA 94720, USA

1. Introduction

Copper-based binary and ternary oxides, due to their p-type conductivity and visible light absorption, have garnered attention as candidate photocathode materials in solar-fuel energy conversion applications such as water splitting and CO_2 reduction.[1] Among them, copper bismuth oxide ($CuBi_2O_4$, denoted as CBO) is compelling as it is a p-type semiconductor with a desirable bandgap (1.67 eV), suitable valence band energy position for CO_2 or water reduction, and relative chemical stability compared to Cu_2O.[2] However, the practical photoelectrochemical (PEC) performance of CBO has been limited. For instance, we show in the current study that it only amounts to several tenths of the theoretical maximum of 4.68 mA cm^{-2} (using AM1.5G solar illumination, with calculations based on absorption coefficient and layer thickness). The performance limitation is commonly attributed to charge carrier losses at bulk and surface defect sites.[2e,3] Although much work has been done to mitigate these loss mechanisms for n-type metal oxides like $BiVO_4$,[4] a well-defined mitigation approach has not yet been developed for p-type materials like CBO.

Surface-related electronic trap states caused by defects or dangling bonds are common for metal oxide semiconductors, especially the ternary oxides, due to unavoidable below-ideal stoichiometry, phase-segregation, oxygen defects, and grain boundaries.[4c,5] Surface states can have significant deleterious effects that cause performance losses in both photovoltage and fill factor values related to fermi level pinning and recombination.[4b,6] Passivation of surface states is thus critically important for practical application of semiconductor materials.[7] However, the passivation layer must also allow charge transport to drive the desired chemistry. The mechanisms of charge transfer at the interface of the semiconductor and its passivation layer include tunneling (which generally requires that the passivation layer be less than 2 nm thick), valence or conduction band conduction, and defect band conduction.[6,8] Given variation in the chemistry of surface recombination sites

and band structures of photoelectrode materials, effective passivation materials must be customized to the semiconductor of interest.[9] Examples of semiconductor/passivation systems developed to date include an ultra-thin Al_2O_3 layer on hematite that passivates surface traps and improves the onset potential by about 100 mV,[2] a 10 nm TiO_2 passivation layer on p-InP photocathodes that improves photovoltage by about 200 mV,[10] and a 20 nm Ga_2O_3 electron-selective layer for Cu_2O that improves the onset potential by about 500 mV.[11]

For a given photocathode, the best passivation material will be one that is capable of transferring electrons, has a Fermi level that is well-matched to that of the photocathode to minimize Schottky barriers, and is stable under the electrolyte and voltage operating conditions. However, the passivation materials developed to date have been mostly limited to simple binary materials, severely limiting the tuning of electronic properties to meet specific requirements. A more extensive exploration of multi-component metal oxide passivation materials allowing for precise tailoring of the Fermi level is necessary. Thus, effective p-type passivation will require new strategies for the discovery and development of new passivation materials.

High-throughput methodology is a powerful technique for materials discovery and optimization, and has been developed to study both complete devices and subcomponents for photovoltaics, fuel cells, batteries, etc.[12] Previously, dispensing and scanning electrochemical systems were used to study the incorporation of 22 different transition and post-transition metals (M) into CuO and CBO to improve PEC performance for photoreduction.[13] Recently, 858 unique Ni-La-Co-Ce quaternary oxide films (286 compositions, each at three loadings) were coated onto a uniform $BiVO_4$ film by inkjet printing, and scanning droplet cell (SDC) PEC measurements were used to provide robust, high-throughput identification of the metal oxide coating that best enhanced photoelectrocatalytic activity for the oxygen evolution reaction.[14]

In this work, high-throughput methodology was applied for preparation and evaluation of semiconductor/passivation assemblies as photocathodes. A library of Y-La-Cu-Ti oxide with 858 discrete coatings was applied to a uniform 10 cm × 10 cm CBO thin film using inkjet-printing. SDC electrochemical results indicated that the $Cu_xTi_yO_z$ ternary oxide coatings exhibited composition-dependent improvement of PEC performance with optimal coatings far outperforming those of the binary oxides. To further investigate the composition-dependent performance and working mechanism, a layer of $Cu_xTi_yO_z$ with gradient Cu:Ti molar ratio (from 0.1 to 4) was deposited onto a CBO thin film using reactive co-sputtering. Both SDC and conventional PEC measurements indicated optimization of PEC performance with a Cu:Ti ratio around 1.5. XPS characterization of the band alignment revealed a gradient of fermi level positions from n-TiO_2 to p-CuO, allowing engineering of the fermi level position of the overlayer by minimizing barriers and allowing for electron transport from the conduction band of CBO. Furthermore, we demonstrate that $Cu_{1.5}TiO_z$ passivates surface defects on CBO, thereby reducing Fermi level pinning and increasing photovoltage while also increasing the lifetime of photogenerated charge carriers.

This work demonstrates a new three-step framework for streamlined discovery and optimization of passivation materials: i) high-throughput inkjet printing of diverse composition spaces to identify systems with ideal properties, ii) combinatorial sputtering of promising composition systems to identify composition–performance trends with more conformal coatings, and iii) detailed multi-modal characterization of electronic structure and photophysics to identify the underlying mechanisms of composition-tuned performance. While these methods need to be applied individually to each semiconductor light absorber of interest, the suite of techniques can rapidly identify high-performance coatings and greatly accelerate the discovery, follow-up, and fundamental understanding phases of interface science research.

2. Results and Discussion

2.1. Initial Characterization of Surface Defects in Sputtered CBO

CBO thin films were grown by reactive co-sputtering on FTO glass substrates, as shown in **Figure 1**a, using metallic Cu and Bi targets operated with RF sputtering powers of 20 and 25 W, respectively. Plan-view SEM images of the resultant film revealed a homogenous, compact layer with granular morphology and uniform grain size around 280 nm, as shown in Figure 1b. 2D XRD shown in Figure 1c was performed to investigate the crystallinity of the CBO film. The sharp and strong Bragg reflection rings without intensity variation indicate the polycrystalline nature of the film. The integrated diffraction profile (Figure 1d) indicates that all peaks are well-matched to those of CBO (Kusachiite, JCPDS 42–0334) and FTO substrate with no other contaminant phases detected. Likewise, the Raman spectrum shown in Figure 1e is indicative of phase-pure CBO.[5a,15]

Transient open-circuit potential (TOCP) measurements reveal the existence of deleterious surface states in bare CBO.[16] TOCP was measured using a continuous white light bias and a pulsed blue light (340 nm) with 200 ms on and 800 ms off times. Under white light illumination, a steady OCP was recorded from the photocathode, as shown in Figure 1f. Initiated by the pulsed blue light, the OCP exhibits a sharp increase until reaching a maximum and then a slow decrease. The initial rise is due to the accumulation of photogenerated minority electrons and the resultant shift of the quasi-fermi level. The slow decrease in OCP is related to electron trapping and recombination processes arising from a mixture of surface and bulk defect states. This claim is supported by the change in the TOCP profile when the blue light intensity is increased from 0.61 to 9.8 mW cm^{-2}, as shown in Figure 1f. At higher powers, defect state saturation reduces recombination. When the blue light is shuttered, the OCP immediately drops, dipping below the original level before fully recovering. The sharp drop is due to rapid recombination of accumulated carriers. The existence of surface defect states has a negative impact on the maximum achievable photovoltage and fill factor due to Fermi level pinning and recombination, respectively. Therefore, identifying an efficient passivation layer is of critical importance for practical application of CBO photocathodes.

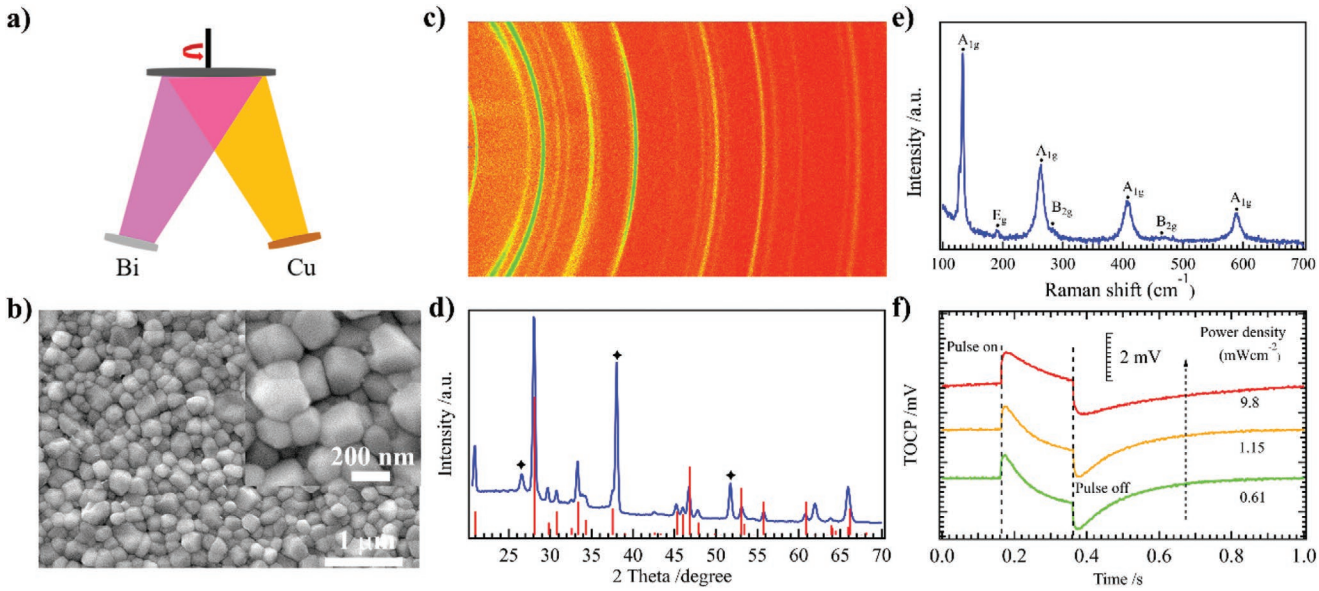

Figure 1. a) Schematic of the deposition of CBO film by co-sputtering method; b) SEM image of as-prepared CBO film on FTO substrate; c) 2D X-ray diffraction pattern and d) integrated diffraction profile with red line and black stars corresponding to CBO and FTO substrate, respectively; e) Raman spectrum with labeled modes of CBO; f) transient open-circuit potential measurements of CBO film under continuous white light bias and pulsed blue light with variable density in 0.1 M $KHCO_3$.

2.2. High-Throughput Discovery of Defect Passivation and Charge Transport Layers

The design of an ideal passivation material for p-type photocathodes should include three criteria: 1) a Fermi level that is well-matched to that of the photocathode to minimize barrier introduction, 2) selective electron transport through proper alignment of the valence and conduction bands, and 3) stability under the measured potential range and reaction environment.[6] Although TiO_2 is a common overlayer choice due to its stability and electron transfer ability,[10,17] it has poor performance on CBO. As shown in Figure S1, Supporting Information, even an ALD-grown TiO_2 overlayer with thickness of just 2 nm results in a decrease of the photocurrent by 33% of its original value (measured at 0.4 V_{RHE}). This decrease is due to the Fermi level of TiO_2 (3.67–4.3 eV)[18] being much lower than that of CBO (4.6–4.7 eV),[5a] which results in an electron transport barrier across the CBO/TiO_2 interface. To satisfy all three aforementioned design criteria, we instead investigate multi-component metal oxides as candidate overlayers. The electronic properties of these materials can be tuned through variation of composition, which makes it possible to design and synthesize passivation materials with a tailored Fermi level for a given photocathode. To that end, data-driven high-throughput techniques were employed to rapidly screen multi-component metal oxide compositions containing up to four elements for optimization of PEC performance.

The pseudo-quaternary oxide library of Y-La-Cu-Ti containing 286 unique compositions, with each composition replicated at three different loadings, was coated by inkjet-printing onto a uniform 10 cm × 10 cm CBO film. Figure S2, Supporting Information, shows a photograph of the library on CBO, with regions L1, L2, and L3 containing loading amounts of 0.8, 1.9, and 3.8 nmol mm^{-2}, respectively. For each composition, *J–V* characteristics were tested by SDC measurements. The electron scavenger was included to reduce convoluting effects from surface catalytic activity for more challenging chemistries such as CO_2 reduction. While we evaluated the PEC performance using a variety of metrics, including onset potential, saturation current, and fill factor, we found that the photocurrent at different applied potentials was an appropriate metric for evaluating relative performance of the various compositions.

The performance of the entire pseudo-quaternary composition space is mapped using three connected sets of four pseudo-ternary triangles (**Figure 2**a). The first set of four triangles comprises the four faces of the outer shell of a tetrahedron. The second and third set of four triangles show the inner shells, where each composition contains at least 10% and 20% of each element, respectively. The maps of net photocurrent at 600 mV versus RHE as a function of composition reveal that the Cu:Ti oxide pseudo-binary line (highlighted by the fuchsia outline) with highest performance contains compositions close to TiO_2. The toggled illumination curve for the return anodic sweeps for the L2 loading of $Cu_{30}Ti_{70}O_x$ is shown in Figure 2b. The negative photocurrent was consistent with p-type conductivity of CBO and the transient current further confirmed the existence of surface defect states. With chemical stability in mind, we elected to further investigate, scale-up, and optimize the $Cu_xTi_yO_z$ composition, given the inherent stability of TiO_2.

Although inkjet printing offers rapid preparation of multi-element libraries, sputtering provides more conformal coating of the semiconductor and is preferred for fabrication of large-area devices. As such, we evaluated a $Cu_xTi_yO_z$ overlayer grown by sputtering to confirm the inkjet findings. $Cu_xTi_yO_z$ coatings with Cu:Ti ratio gradient were achieved by reactive co-sputtering onto 10 cm × 10 cm CBO films with no sample rotation. Figure S3a, Supporting Information, shows an SEM image of CBO with $Cu_xTi_yO_z$ overlayer, demonstrating that there is no

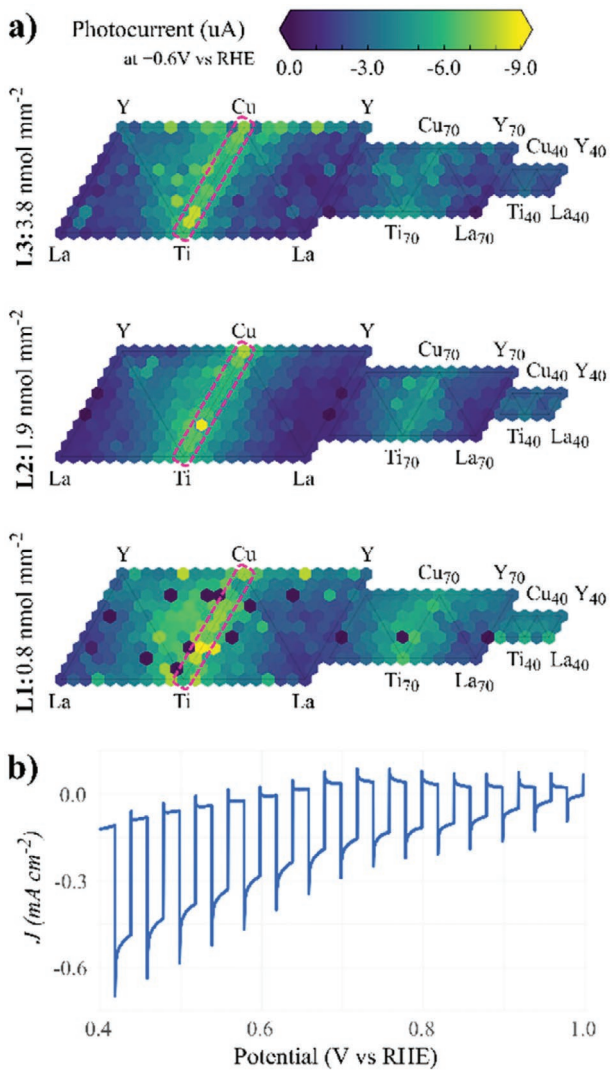

Figure 2. Composition maps of net photocurrent for three different loadings of: a) La-Y-Ti-Cu oxide. The full pseudo-quaternary composition space is shown as the unwrapped set of pseudo-ternary faces with the three sets of four faces arising from the three concentric shells of the tetrahedral composition plot. b) The toggled illumination voltammogram from the return anodic sweep from 0.4 to 1.0 V versus RHE for the L2 $Cu_{30}Ti_{70}O_x$ sample.

visible change in CBO morphology after deposition. The overlayer fully covers the CBO and forms a conformal CBO/$Cu_xTi_yO_z$ film. High-resolution cross-section EDX mapping of CBO/$Cu_xTi_yO_z$, shown in Figure S3b, Supporting Information, reveals a CBO thickness of 160 nm with uniform composition and a homogenous $Cu_xTi_yO_z$ layer with thickness around 8 nm.

The elemental composition of the 10 cm × 10 cm CBO film was measured using X-ray fluorescence (XRF) mapping[14] and results were confirmed with ICP-MS by etching small portions of the film with nitric acid. As shown in **Figure 3**a, the Bi:Cu ratio increased radially from 2.4 to 2.8 across the film dimensions, due to the relative position of the sputtering guns and sample rotation during deposition. The radial Bi:Cu gradient is highlighted with an arrow. This serendipitous heterogeneity provided the opportunity to identify the optimized Bi:Cu ratio of CBO along with the optimized Cu:Ti ratio of the $Cu_xTi_yO_z$ overlayer. For the CBO/$Cu_xTi_yO_z$ sample, XRF mapping revealed that the Cu:Ti ratio ranged from 0.1 to 4 diagonally across the film. The linear Cu:Ti gradient is highlighted with an arrow in Figure 3b.

PEC performance maps of CBO and CBO/$Cu_xTi_yO_z$ films were assessed with SDC measurements, vide supra. Resultant photocurrent maps of the two films at fixed potential (0.8 V_{RHE}) are shown in Figure 3c,d. For bare CBO, the photocurrent is approximately –0.24 mA cm^{-2} across the majority of the film, with performance decreasing near the Bi-rich edges. A slight radial pattern is distinguishable. Upon addition of the $Cu_xTi_yO_z$ overlayer (Figure 3d), the photocurrent varies both radially and linearly across the sample, indicating that the passivated film performance depends upon both the Bi:Cu ratio of the CBO and the Cu:Ti ratio of the overlayer. At 0.8 V_{RHE}, the best performance is obtained at the intersection of the Bi:Cu ratio of 2.5 ± 0.1 and a Cu:Ti ratio of 1.5 ± 0.6, reaching a photocurrent of –0.44 mA cm^{-2}.

The photocurrent of CBO and CBO/$Cu_xTi_yO_z$ were mapped at three potentials (0.4, 0.6, and 0.8 V_{RHE}), as displayed in Figure S4, Supporting Information. At relatively positive potentials (lower applied potential), photocarriers accumulate in the near surface region due to weaker electric fields and more readily recombine due to a higher concentration of photoholes, making the influence of defect recombination more apparent. For instance, for bare CBO at 0.4 V_{RHE} (higher applied potential), the photocurrent appears to be relatively uniform across the film, reaching a maximum of –2.1 mA cm^{-2}. However, when the potential is increased to 0.6 V_{RHE} and then to 0.8 V_{RHE} (lower applied voltage), the photocurrent decreases across the entire film, but more strongly at the Bi-rich edges. Thus, the effect of composition ratio on performance becomes more easily observable.

Onset potential mapping was also used to evaluate the best overlayer composition.[7,8e] Figure 3e,f shows the onset potential maps of bare CBO and CBO/$Cu_xTi_yO_z$, respectively. For bare CBO, as analyzed above and reported previously,[2e,5a] the Bi-rich edges show lower onset potentials. This result is consistent with Bi-rich regions containing a higher concentration of defects, thus lowering the photovoltage through recombination or fermi level pinning. The same observation can be made for the CBO/$Cu_xTi_yO_z$ film; a radial pattern is present with lower onset potentials at the Bi-rich edges, again suggesting that performance is more strongly dependent on the radial Bi:Cu ratio of the CBO than the linear Cu:Ti ratio of the overlayer. Overall, the onset potential maps with and without overlayer are quite similar, with a slight increase in onset potential values in the center of the film upon overlayer addition. The best performance is achieved in the CBO/$Cu_xTi_yO_z$ sample with a Cu:Bi ratio around 2.5 ± 0.1 and a Cu:Ti ratio of 1.4 ± 0.5. These results are in excellent agreement with the optimal ratios identified with photocurrent mapping.

The thickness of the overlayer also has a great effect on the performance of the photocathode material. Comparing the photocurrent maps at 0.6 V_{RHE} for CBO/$Cu_xTi_yO_z$ with overlayer thickness of 8 nm (**Figure 4**a) and 24 nm (Figure 4b), the thinner overlayer consistently shows higher photocurrents over the entire composition range. The photocurrent map for the

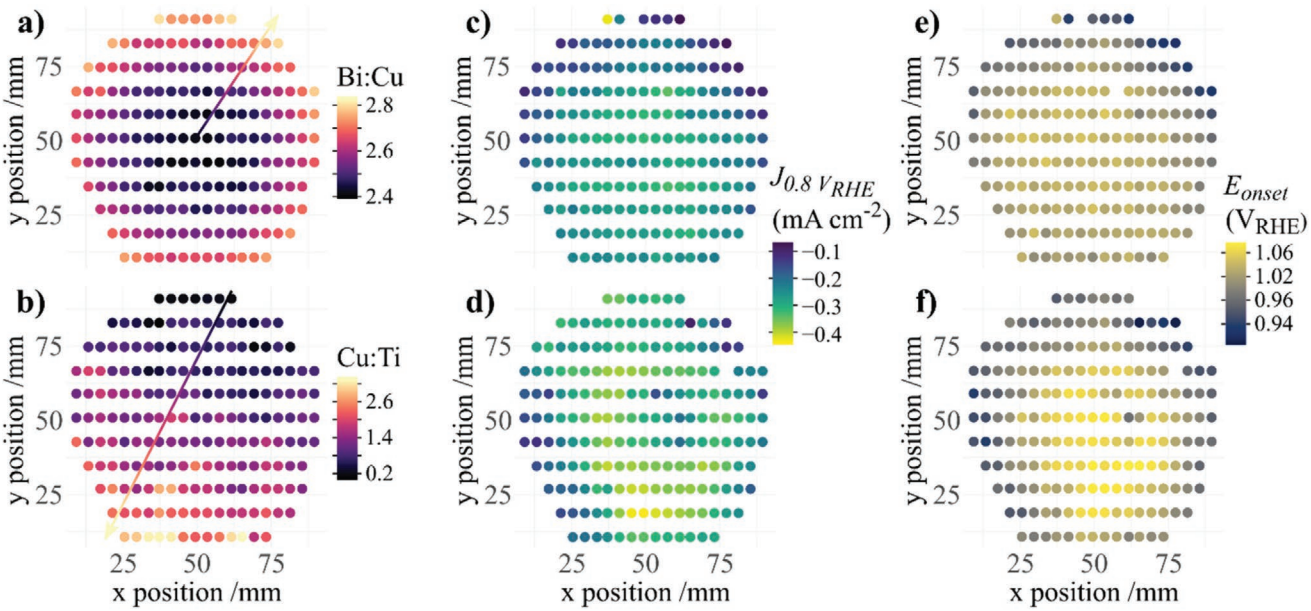

Figure 3. XRF elemental composition maps of a) 10 cm × 10 cm CBO and b) CBO/$Cu_xTi_yO_z$ films with corresponding photocurrent (c,d) and onset potential (e,f) maps. The photocurrent at fixed potential (0.8 V_{RHE}) was measured by high-throughput SDC under 455 nm Doric LED illumination in 0.1 M $KHCO_3$ with 0.1 M $Na_2S_2O_8$ (pH = 8.2). The photocurrent onset potential ($J < -0.01$ mA cm^{-2}) was extracted from chopped illumination CV data.

sample with the thicker overlayer shows a simple radial pattern, as shown in Figure 4b, reflecting a strong dependence on the Bi:Cu ratio of the CBO but not the Cu:Ti ratio of the overlayer. Thus, the sample with thinner overlayer is more sensitive to the Cu:Ti ratio of the overlayer.

2.3. Scale-Up, Characterization, and Mechanistic Understanding

Having identified high performance for coatings with thickness of approximately 8 nm and Cu:Ti ratio of 1.5 ± 0.6, we fabricated large-area (7.5 cm × 5 cm) uniform CBO/$Cu_{1.5}TiO_z$ to investigate the origins of the performance enhancement. A CBO film was grown on FTO by sputtering, annealed at 550 °C for 2 h in air, and then split in half. $Cu_{1.5}TiO_z$ was deposited on one half and both pieces were further annealed at 500 °C for 30 min in air, so any differences in performance could be confidently assigned to the presence of the overlayer. The J–V response of CBO and CBO/$Cu_{1.5}TiO_z$ under front-side illumination with blue LED (365 nm) at 88 mW cm^{-2} (2.45 suns equivalent) in 0.1 M $KHCO_3$ with 0.1 M $Na_2S_2O_8$ (pH = 8.4) is displayed in **Figure 5**a. The CBO/$Cu_{1.5}TiO_x$ showed a significantly improved photocurrent onset potential compared to that of bare CBO (a 110 mV shift from 1.00 to 1.11 V_{RHE}) as measured at 0.05 mA cm^{-2}. Also, the photocurrent density increased to −0.55 mA cm^{-2} at 0.88 V_{RHE}, which is 2.8 times higher than bare CBO (−0.2 mA cm^{-2}) under the same applied potential. When the applied potential was decreased to 0.48 V_{RHE}, the photocurrent became similar with that of bare CBO (−1.27 mA cm^{-2}). Taken together, the photocurrent results

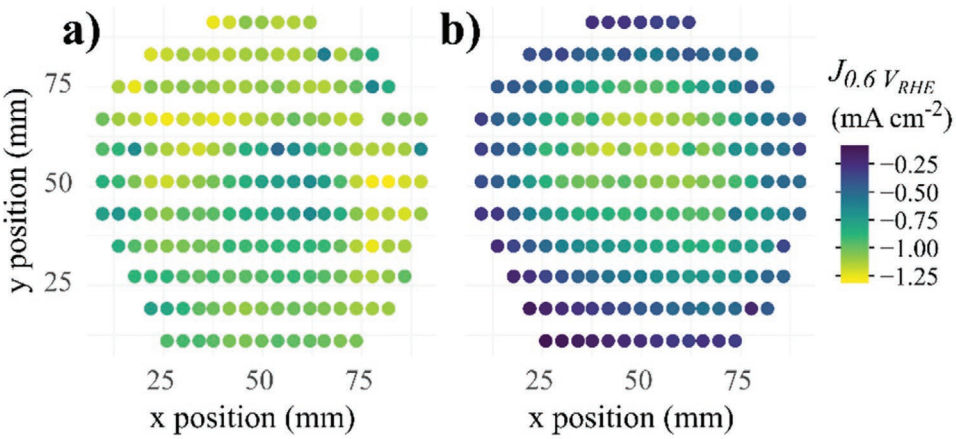

Figure 4. High-throughput photocurrent maps of CBO/$Cu_xTi_yO_Z$ samples at 0.6 VRHE with different overlayer thicknesses, a) 8 nm and b) 24 nm, respectively.

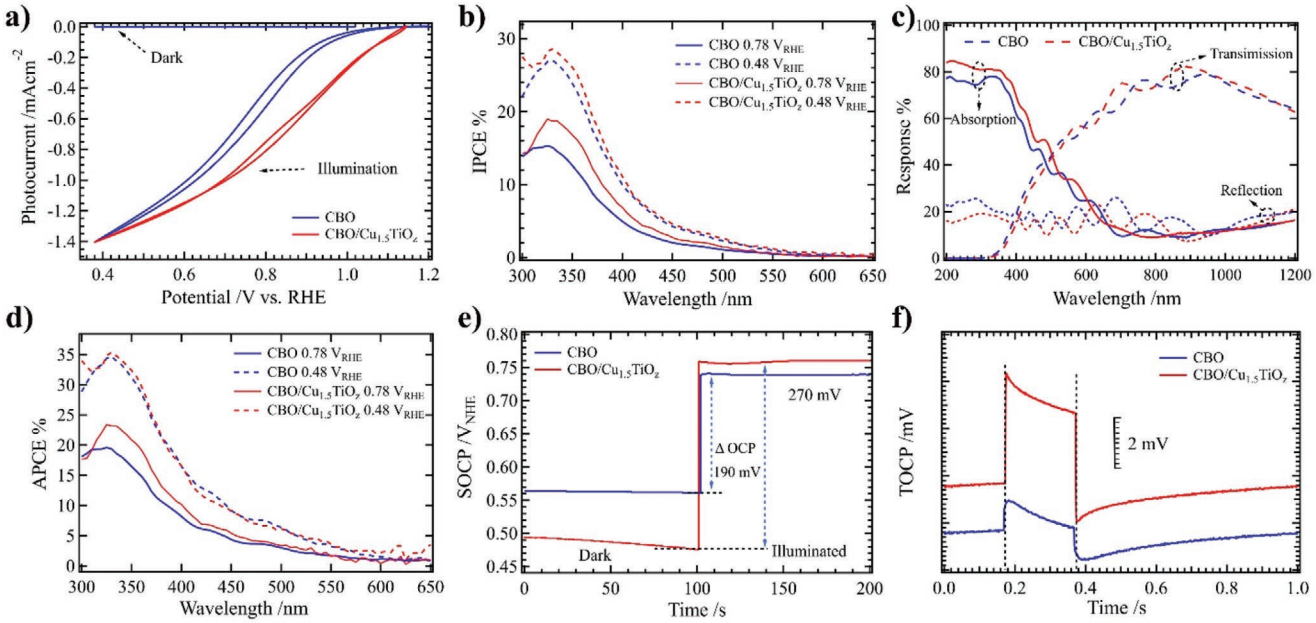

Figure 5. a) The *J–V* curves of CBO with (red) or without (blue) $Cu_{1.5}TiO_z$ overlayer under front-side illumination with blue LED (365 nm) at 88 mW cm^{-2} in 0.1 M $KHCO_3$ with 0.1 M $Na_2S_2O_8$ (pH = 8.2); b) IPCE spectra of CBO and CBO/$Cu_{1.5}TiO_z$ samples measured at 0.48 and 0.78 V_{RHE}; c) transmission, reflection, and absorption spectroscopy of CBO film with (red) or without (blue) $Cu_{1.5}TiO_z$ overlayer; d) APCE of CBO and CBO/$Cu_{1.5}TiO_z$ samples calculated from IPCE and related UV–vis spectra; steady-state (e) and transient (f) open-circuit potential measurements of CBO and CBO/$Cu_{1.5}TiO_z$ samples in the dark and under illumination in CO_2-purged $KHCO_3$ (0.1 M, pH = 6.8).

reveal a 32% improvement in fill factor with overlayer addition but no increase in saturation current.

The origin of performance enhancement upon overlayer addition was also investigated, particularly whether the improvement in photocurrent is due to increased light harvesting of CBO/$Cu_{1.5}TiO_z$ as $Cu_{1.5}TiO_z$ is light brown by eye. Indeed, the UV–vis absorption spectra, shown in Figure 5c, demonstrate a slight increase in absorption upon $Cu_{1.5}TiO_z$ overlayer addition. In the reflection spectrum, the increase in sample thickness and change in dielectric properties by $Cu_{1.5}TiO_z$ modifies the interference fringes. IPCE as shown in Figure 5b reveals the $Cu_{1.5}TiO_z$ overlayer does not change the onset wavelength (≈600 nm) but improves the IPCE, particularly at 0.78 V_{RHE} but less so at 0.48 V_{RHE}. This is consistent with an improved fill factor. If the performance enhancement is only due to enhanced light absorption, the absorbed photon conversion efficiency (APCE) should remain unchanged.[19] However, as shown in Figure 5d, upon overlayer addition, the APCE improves by 15.5% at 0.78 V_{RHE}, and this value decreases to 4.2% as the potential negatively shifts to 0.48 V_{RHE}. This result indicates that the improvement in PEC performance upon overlayer addition is due to improved charge carrier collection efficiency rather than enhanced light absorption.[5a,20]

Steady-state open-circuit potential (SOCP) measurement, which reflects the difference in Fermi level of the dry semiconductor and the redox potential of the electrolyte, was carried out in the dark and under illumination.[2c,2f,21] As shown in Figure 5e, in the dark, the CBO shows a positive SOCP around 0.56 V. This SOCP was shifted by 70 mV after overlayer addition, which we attribute to passivation of surface defects.[8d] As depicted in **Figure 6**a for a fully passivated surface without illumination, the Fermi level of the semiconductor is in equilibrium with the redox potential of the electrolyte, resulting in downward band bending at the interface as the Fermi level of CBO is below that of water. However, the existence of surface states causes Fermi level pinning which reduces the degree of band bending and thus lowers the SOCP, Figure 6b.

Under illumination, Figure 5e, both samples show a positive shift in SOCP, but the change is greater for CBO/$Cu_{1.5}TiO_z$ than for CBO. The change of SOCP (ΔSOCP) upon illumination reflects the change in the Fermi level due to the presence of photogenerated carriers. CBO/$Cu_{1.5}TiO_z$ generated a ΔSOCP of about 270 mV, which is 80 mV larger than that of bare CBO and suggests reduced recombination rates arising from surface passivation by $Cu_{1.5}TiO_z$. Although ΔSOCP is different from the photovoltage (V_{ph}), which is defined as the difference between the quasi-Fermi levels of the electrons ($E_{f,n}$) and holes ($E_{f,p}$), ΔSOCP is expected to track V_{ph}.[8d] As shown in Figure 6c,d, the difference between the Fermi level and the valance band is defined as Δ_{FV}. The degree of band bending is then determined using surface Δ_{FV} ($\Delta_{FV-surf}$) and bulk Δ_{FV} ($\Delta_{FV-bulk}$) according to Equation (1).[22]

$$V_{bb} = \Delta_{FV-surf} - \Delta_{FV-bulk} \quad (1)$$

where V_{bb} is the thermodynamic limit of the achievable V_{ph}. If the doping level of a semiconductor is given, the $\Delta_{FV-bulk}$ would be fixed. To maximize V_{ph}, the $\Delta_{FV-surf}$ should be improved. However, the existence of surface states is detrimental to V_{ph} because it is decreased by pinning of the Fermi level.

On the other hand, under open circuit conditions, the buildup and decay of V_{ph} are due to dissipation and accumulation

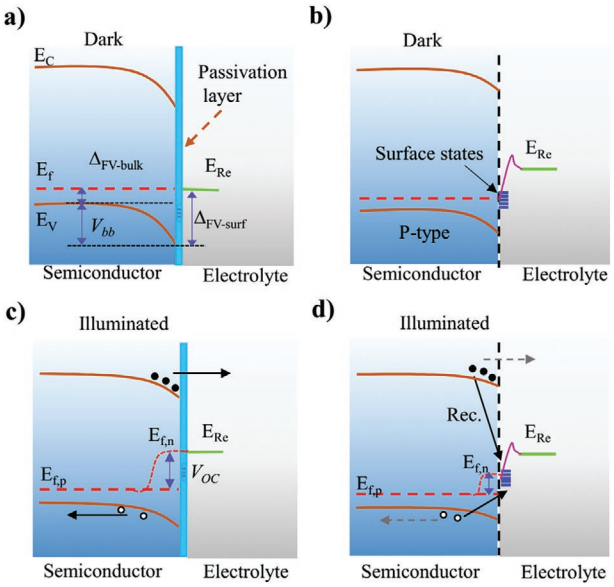

Figure 6. Band diagrams of CBO/electrolyte interface under open-circuit conditions, with and without passivation layer. In the dark and with passivation layer, the degree of band banding is determined by the difference of the Fermi level and valance band edge in the body and surface (a); surface states contribute to pinning the Fermi level relative to the band edge position, reducing the degree of band banding (b); under illumination, photogenerated charges split the Fermi levels of electrons ($E_{f,n}$) and holes ($E_{f,p}$) and produce a photovoltage on the surface (c); the CBO with surface states produces a smaller photovoltage (d).

of photogenerated charge carriers in the photoelectrode by Equations (2) and (3).

$$V_{ph} = E_{f,n} - E_{f,p} = \frac{kT}{q} Ln \frac{n}{p} \approx \frac{kT}{q} Ln \frac{\Delta n}{N_d} \tag{2}$$

$$\frac{\partial \Delta n}{\partial t} = G - R \tag{3}$$

Here, as a p-type semiconductor, the density of majority carriers (holes) is close to the p-type doping density (N_d); the density of minority carriers (electrons) is equal to the net generated electrons Δn; G and R stand for the generation and recombination rate of electrons, respectively.

Because there is no significant improvement in light absorption upon overlayer addition, G is constant between the samples and any difference in V_{ph} should be caused by a change in R. To confirm this assumption, the transient OCP was examined immediately after the introduction of pulsed light. As shown in Figure 5f, upon illumination, both samples show increased OCP as G is increased, but bare CBO increases more slowly than CBO/$Cu_{1.5}TiO_z$ and the final TOCP is much lower. Also, over the 200 ms light pulse duration, the OCP in bare CBO decreases more rapidly than the passivated sample. This result indicates that the R for bare CBO is much higher than that for CBO/$Cu_{1.5}TiO_z$. As soon as the pulse is off, the OCP response for both samples dips below that of the original baseline as a result of recombination of accumulated charge carriers. Additionally, as shown in Figure 1d and Figure S5, Supporting Information, both samples show an increased ΔTOCP as the pulse power density is increased, but the value of CBO/$Cu_{1.5}TiO_z$ is four times that of CBO. From these results we can conclude that the overlayer effectively reduces R through surface passivation.

Further confirmation of these findings through direct measurement of the recombination of photoexcited carriers in CBO and CBO/$Cu_{1.5}TiO_z$ was evaluated by transient transmission and reflection spectroscopies. Differential transmission (dT) and differential reflection spectra (dR) of both CBO and CBO/$Cu_{1.5}TiO_z$ films at various pump-probe delays are provided for reference in Figure S6, Supporting Information. **Figure 7**a shows the differential transmission (dT) and differential reflection (dR) spectra of the CBO film at various time delays following optical excitation by a 350 nm, 100 fs pulse. The shape of the differential signals is related to a modification of the optical properties (i.e., the complex index of refraction) of the semiconductor as a result of the perturbation of the charge carrier band populations by the pump pulse.[23] This effect is most clearly evident in the dR spectrum where the thin film interference fringes dominate due to a modification of the refractive index. Thus, without significant optical modeling efforts, which are beyond the scope of the current report, the technique probes the existence of photoexcited carriers but not specific carriers such as valence band holes or conduction band electrons as commonly asserted in the literature.[24] Typically, temperature-induced changes in optical properties due to laser-induced heating from carrier recombination are of critical importance to

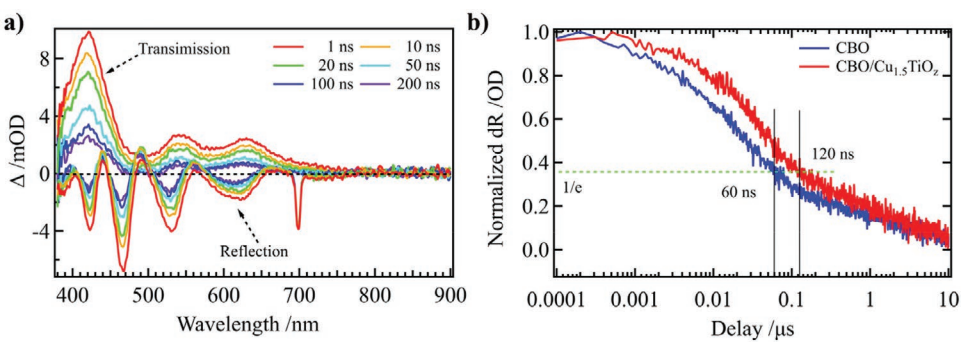

Figure 7. a) Differential transmission (dT) and differential reflection (dR) spectra of CBO film at various pump-probe delays. Excitation wavelength: 350 nm, power: 0.8 uJ per pulse, beam diameter: 0.3 mm; b) time dependence of dR signal at 540 nm probe wavelength for both CBO (blue) and CBO/$Cu_{1.5}TiO_z$ films.

deconvolve in order to ascertain information related to excited carrier populations.[25] In this case, however, because we are comparing only CBO with and without $Cu_{1.5}TiO_z$, any changes in dynamics can be attributed to a change in electronic-related components as the thermal properties of the films are assumed to be effectively identical.

Under 350 nm illumination, photogenerated carriers are expected to be primarily located at the surface of the semiconductor and reflection mode is more sensitive to interfacial dynamics than transmission mode. Therefore, carrier lifetime was compared using the reflection spectra. The time dependence of the dR signal of CBO and CBO/$Cu_{1.5}TiO_z$ for the 540 nm probe wavelength is displayed in Figure 7b. It can be seen that addition of the passivation layer slows the recombination of charge carriers and results in a doubling of the 1/e value: the 1/e value for CBO is 60 ns while the 1/e value for CBO/$Cu_{1.5}TiO_z$ is 120 ns.

2.4. Band Alignment of CBO/Passivation Layer Heterojunctions

Taken together, all results indicate that the engineered $Cu_{1.5}TiO_z$ overlayer effectively passivates surface states on the CBO film while maintaining effective charge transfer at the interface. As discussed in the introduction, charge carrier transfer at the interface of the photocathode and passivation layer can occur through tunneling or band conduction. In this case, because the overlayer thickness is approximately 8 nm, tunneling can be ruled out. Therefore, the conduction mechanism is likely to function by selective electron transport through the conduction band of $Cu_{1.5}TiO_z$. However, to support this mechanism, the band energetics of CBO and the various passivation layers must be thoroughly examined.

We therefore investigated the band alignment of the work function and Fermi level position of the sputter-deposited $Cu_xTi_yO_z$ sample with Cu:Ti ratios ranging from 0.1 to 4. Figure S7a, Supporting Information, shows the composition map of the $Cu_xTi_yO_z$ overlayer as measured by XRF, with six selected points also analyzed by XPS. The valence band edge measurements shown in Figure S7b, Supporting Information, indicate that addition of Cu significantly raises the valence band from that of TiO_2 toward that of CuO. The valence band data also suggest the conversion of the layer from n-type TiO_2 to p-type CuO with a gradient of doping in between. This result is further confirmed from examination of the Ti 2p core level spectra, which shift to lower binding energies with increasing Cu content. As the Fermi level of $Cu_xTi_yO_z$ moves closer to the valence band with increasing Cu, the Ti 2p levels appears to shift to lower binding energies as the Fermi level of the material is in equilibrium with the Fermi level of the detector (Figure S8, Supporting Information). Secondary electron cut-off measurements shown in Figure S7c, Supporting Information, reveal that the work function ranges from 4.22 to 4.74 eV as the Cu:Ti increases from 0.2 to 2.6, further demonstrating Cu-dependent tuning of the Fermi level. The apparent gradient-doping transition from n-TiO_2 to p-CuO may be supported by several stable phases of Cu:Ti with intermediate composition, including: Cu_2Ti_4O, Cu_3Ti_3O, and Cu_3TiO_4. The optimized 1.5 Cu:Ti ratio (similar to point 5) resulted in a work function of 4.50 eV, which is well-matched to that of CBO (4.60 eV).

To construct vacuum band energetics diagrams for our heterojunction systems, we measured and combined the bandgap, work function, and Fermi level position relative to the valence band edge for each of our component materials.[26] To characterize the bandgaps, uniform thin films of CBO, CuO, TiO_2, and $Cu_{1.5}TiO_z$ were fabricated for analysis by UV–vis. Transmission and reflection intensities for CuO and $Cu_{1.5}TiO_z$ are displayed in Figure S7d, Supporting Information, and Tauc plot was constructed based on absorption coefficients. The optical band gaps of CBO, CuO, TiO_2, and $Cu_{1.5}TiO_z$ were determined to be 1.8, 1.5, 3.2, and 1.6 eV, respectively, as shown in Figure S7e, Supporting Information. From this information, the relative band energy diagram of CBO with TiO_2, CuO, and $Cu_{1.5}TiO_z$ before contact was constructed, as shown in Figure S7f, Supporting Information. The red dashed line denotes the redox potential of the electrolyte (E_{re}) and the green dashed lines indicate the various Fermi levels (E_F).

Figure 8 shows band alignments of p-CBO/n-TiO_2, p-CBO/p-CuO, and p-CBO/p-$Cu_{1.5}TiO_z$ after formation of the solid heterojunction and solid–liquid junction in the dark. Since the passivation layer is only 8 nm in thickness, the depletion space should extend to CBO. For the CBO/TiO_2 interface, Figure 8a, the relative positions of the work functions after Fermi level equilibration makes it favorable for photogenerated electrons to move from the conduction band of CBO into that of TiO_2. However, Fermi level equilibration with the solution results in significant upward band banding at the TiO_2 solution interface, which blocks electron transfer. For the CBO/CuO interface, Figure 8b, a type-II heterojunction will form,[27] which will inhibit electron transfer from CBO to CuO due to energetic barrier at the interface. This observation is consistent with our previous report in which we found that CuO can be used as a hole-selective contact at the CBO interface to improve hole collection efficiency and reduce recombination.[5a] In the case of $Cu_{1.5}TiO_z$, a type-II heterojunction will also form at the CBO/$Cu_{1.5}TiO_z$ interface, as illustrated in Figure 8c, yet the Fermi level is well-aligned with the underlying CBO, resulting in no energetic barrier for photoelectrons. Furthermore, Fermi level equilibration at the $Cu_{1.5}TiO_z$ solution interface results in downward band bending, helping to drive the photoelectrons toward the surface, while the mismatched valance band blocks hole transfer at the interface. Thus, the optimized CBO/$Cu_{1.5}TiO_z$ interface is uniquely suited to meet the first two criteria of an efficient passivation layer: a Fermi level that is well-matched to that of the photocathode to minimize barrier introduction and selective electron transport through proper alignment of the valence and conduction bands.

The third and final criterion, stability, is critical for real world material applications. To test the stability of the CBO photocathode before and after deposition of $Cu_{1.5}TiO_z$, photocurrent was measured at 0.8 V_{RHE} under blue LED illumination over the course of 2 h, Figure S9, Supporting Information. CBO shows relative stability for the first 10 min, followed by continuously decreasing photocurrent for the remainder of the 120 min measurement duration. By the 120th min, the photocurrent is roughly one-half of its initial value. On the other hand, CBO/$Cu_{1.5}TiO_z$ shows relative stability for the first 20 min,

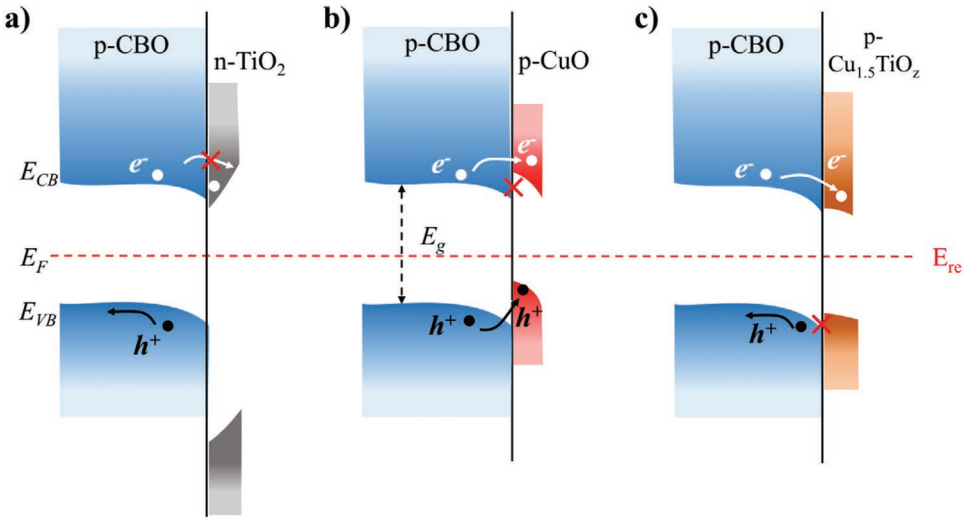

Figure 8. a) Band alignments at interface of CBO with TiO_2, b) CBO with CuO, and c) CBO with $Cu_{1.5}TiO_z$, in electrolyte containing 0.1 M $KHCO_3$ and 0.1 M $Na_2S_2O_8$ (pH = 8.2) with reduction potential (E_{re}) at 0.12 V_{RHE} (−4.56 V_{vac}).

followed by photocurrent increase until the 75th min, and then photocurrent decrease to the 120th min. By the 120th min, the photocurrent is one-third more than its original value. These observations may be related to some decomposition of the $Cu_{1.5}TiO_z$ surface coating under reducing conditions and formation of metallic copper surface species, which could improve the surface activity. Future work may focus on gaining further stability enhancements with the inclusions of a metallic catalyst to help reduce lingering charge in the $Cu_{1.5}TiO_z$, which may cause performance losses due to Cu^{2+} reduction.

3. Conclusion

In summary, high-throughput fabrication and evaluation methods, including inkjet-printing, scanning drop electrochemical cell, and XRF composition mapping, were leveraged to efficiently identify and optimize multi-component passivation materials for p-type CBO. The photocurrent map of the pseudo-quaternary oxide library with 858 unique composition-loading coatings on CBO clearly demonstrated the advantage of Ti-rich $Cu_xTi_yO_z$ overlayers. This result was further confirmed and investigated using a sputtered CBO/$Cu_xTi_yO_z$ photocathode with gradient Cu:Ti ratio. Photocurrent and onset potential maps show clearly improved performance when the Bi:Cu ratio is around 2.51 ± 0.05 and the Cu:Ti ratio is around 1.5 ± 0.6. At these optimal compositions, the onset potential is shifted by 110 mV and the photocurrent is increased 2.8-fold at 0.88 V_{RHE}, as compared to that of bare CBO. A 15.5% improvement in APCE at 0.78 V_{RHE} indicates that improved PEC performance upon overlayer addition is mostly due to enhanced charge carrier collection efficiency. Steady and transient open-circuit potential measurements revealed that $Cu_xTi_yO_z$ works as a passivation layer, which suppresses carrier recombination and reduces Fermi level pinning. Extended carrier decay from transient reflection spectroscopy further confirmed effective surface passivation. XPS characterization revealed that the Fermi level and valance band of the $Cu_xTi_yO_z$ film is tuned by adjusting the Cu:Ti ratio. The optimized $Cu_{1.5}TiO_z$ layer forms a type-II heterojunction with CBO, in which it is energetically favorable for photogenerated electrons to be injected from CBO to the conduction band of $Cu_{1.5}TiO_z$ while blocking holes in the valance band of CBO. More broadly, this work demonstrates that rational design of new materials with fermi level engineering is critical to achieve optimized performance of semiconductors in practical applications of solar-fuel energy conversion.

4. Experimental Section

Preparation of CBO Thin Films: Thin film samples of CBO were deposited onto 10 cm × 10 cm fluorine-doped tin oxide (FTO)-coated glass substrates (TCO10-10, Solaronix) by reactive co-sputtering in a LAB Line sputtering system (Kurt J. Lesker). The working atmosphere consisted of 10 mTorr of Ar (86%) and O_2 (14%), and the substrate was kept at 400 °C while rotating at 10 rpm during the deposition process. Two radio frequency power supplies were separately controlled to manipulate the sputtering powers on circular Cu and Bi targets (each with 2" diameters). The applied powers were fixed at 20 and 25 W for Cu and Bi, respectively, which translated to a growth rate of 2.7 nm min^{-1}. The as-deposited samples were then annealed at 550 °C for 2 h in air using a box furnace (CBFM518C, Cole Parmer), followed by natural cooling to room temperature.

Synthesis of Pseudo-Quaternary Oxide Libraries: The CBO light absorber plate served as the substrate for depositing an array of metal oxide coatings to create a library of photocathode candidates, as previously described for investigation of integrated photoanode libraries.[14] The composition library of mixed-metal oxide coatings was prepared from combinations of metal oxide precursors for YO_x, LaO_x, CuO_x, and TiO_x. Each combination was synthesized on a CBO-coated plate as discrete library spots with 10 atom% composition steps in each element. Each of the 286 compositions in this quaternary composition space was deposited at three different loadings (designated L1, L2, and L3), as illustrated in Figure S2, Supporting Information. The array of 858 metal oxide samples was deposited by inkjet printing at a resolution of 2880 × 1440 dpi, as described previously.[12a,28] Elemental precursor inks were prepared by mixing 3.33 mmol of each metal precursor with 20 mL of pre-mixed ink base consisting of 13 g Pluronic F127 (Aldrich), 16.0 mL glacial acetic acid (T.J. Baker, Inc.), 3.0 mL of concentrated HNO_3 (EMD), and 1000 mL of 200 proof ethanol (Koptec). The metal

precursors were $Ti(i\text{-}OBu)_4$ (1.2 mL, ≥98.5%, Sigma Aldrich), $Y(NO_3)_3$-$6H_2O$ (1.28 g, 99.8% Sigma Aldrich), $La(NO_3)_3$-$6H_2O$ (1.54 g, 99.999%, Sigma Aldrich), and $Cu(NO_3)_2$-$3H_2O$ (0.828 g, 99.999%, Sigma Aldrich). After inkjet printing the composition-loading library, the inks were dried by heating in air at 40 °C for 20 h, followed by heating at 70 °C for 48 h. The metal precursors were then converted to metal oxides by calcination in an O_2-filled tube furnace using a 5 h ramp to, and 5 h soak at, 350 °C. The oxygen stoichiometry for each sample is not known and thus we refer to samples using the intended cation composition.

Each catalyst sample was synthesized over a 1 mm × 1 mm electrode area containing 0.75 nmol of metal for loading L1, 1.9 nmol of metal for loading L2, and 3.8 nmol of metal for loading L3. The 858 catalyst samples were deposited along with additional duplicate (unused) samples on a square grid with 2 mm pitch. For the coated-CBO library, the array of samples was contained within an 8.8 cm-diameter circle centered on the 10 cm × 10 cm square plate. For each loading, the 286 catalyst compositions were randomly distributed over the grid of sample positions. Consequently, the effect of composition was not convoluted with any spatial or temporal artefacts in the PEC measurements, lending confidence to systematic composition-performance trends.

Deposition of $Cu_xTi_yO_x$ Coatings: Deposition of the $Cu_xTi_yO_x$ coatings onto the CBO film was performed with reactive co-sputtering. To create a gradient Cu:Ti ratio, the location of the Cu target, Ti target, and substrate were fixed at three points of a triangle, and the substrate was kept stationary (no rotation). The applied powers were 10 W and 100 W for Cu and Ti, respectively, which translated to a growth rate of 0.27 nm min^{-1}. The resultant CBO/$Cu_xTi_yO_x$ film was then annealed at 500 °C for 30 min in air.

Sample Characterization: The transition metal compositions of the CBO film were quantified by inductively coupled plasma mass spectrometry (7900 ICP-MS, Agilent) after digesting the films with concentrated nitric acid (Sigma-Aldrich, 225711). The crystalline structure of the samples was analyzed by 2D X-ray diffraction with a Rigaku Smartlab Studio II diffractometer using Cu Kα radiation under PB mode. Hypix-3000 2D detector was fixed at 150 mm from the sample. Raman spectra were recorded using a confocal Raman microscope (LabRam HR, Horiba Jobin Yvon) with a 532 nm laser source. The spectral positions were calibrated by the characteristic Si phonon peak at 520.7 cm^{-1}. Sample morphologies were inspected using a scanning electron microscope (Quanta FEG 250, FEI) with 10 kV acceleration. Grain sizes were analyzed with Nano Measurer 1.2. X-ray photoelectron spectroscopy (XPS) data were acquired by a Kratos Axis Ultra spectrometer, using an Al-Ka source ($h\nu$ = 1486.69 eV) operated at 225 W and a hemispherical electron energy analyzer. XPS binding energy was calibrated using adventitious alkyl carbon signals by shifting the C 1s peak to 284.8 eV. A –10 V potential was applied for the second electron cut-off measurement. Transmission and specular reflection were measured at an 8° incident angle, using a UV–vis spectrometer equipped with an integrating sphere (SolidSpec 3700, Shimazu) from 200–1600 nm. Transient spectroscopy was measured using a Coherent Libra laser (Coherent, CA, USA) with pulse width of 100 fs and repetition rate of 1 KHz. A portion of the 800 nm output was coupled to a Coherent OperA Solo optical parametric amplifier to generate a 350 nm laser pump pulse. A separate portion of the 800 nm output was coupled to a CaF_2 crystal to generate a super-continuum white light probe. An Ultrafast Systems (Sarasota, FL, USA) TA measurement system, which included two fiber-coupled grating spectrometers with Si complementary metal-oxide semiconductor detector arrays, was used for analysis of the 315–800 nm spectral range. The setup was modified such that one detector was used to detect the differential transmission (dT) signal and the other was used for simultaneous collection of the differential reflection (dR) signal.

Scanning Droplet Cell Photoelectrochemical Measurements: PEC experiments were conducted on CBO with coating libraries using previously reported SDC instrumentation, potentiostat (Gamry G 300), and custom automation software.[12a] Figure S10, Supporting Information, shows a cross-sectional diagram of the SDC, which creates a three-electrode cell for each sample, including a Pt wire counter electrode and an Ag/AgCl reference electrode. Contact to the CBO film working electrode was made by adhering Cu tape to the TCO conducting layer along the perimeter of the library. The SDC was operated as a flow cell in which aqueous electrolyte flowed at approximately 10 µL s^{-1}, flushing the active drop volume approximately ten times per second. Experiments were performed with electrolyte containing 0.1 M potassium bicarbonate (pH 7) and 0.1 M sodium persulfate (as the sacrificial electron acceptor).

To enable PEC measurements, a 0.4 mm diameter optical fiber was placed in the central axis of the SDC and terminated approximately 1 mm above the sample, illuminating an approximately 1.5 mm-diameter circle. Illumination experiments were performed using 0.86 mW, 455 nm illumination from a light emitting diode (LED, Doric), toggled on for 0.5 s and off for 0.5 s. The illumination power was measured by placing the operational SDC on a quartz plate and collecting the transmitted light with an optical meter (Newport Corporation, 1918-R) configured with a silicon–UV enhanced photodetector (Newport Corporation, 818-UV). During illumination toggling, a single cyclic voltammogram cycle was collected using a sweep rate of 40 mV s^{-1}. The sweep range of the CV was +1.0 to +0.2 V for the Y-La-Cu-Ti oxide library and +1.2 to +0.4 V versus RHE for the sputtered composition gradient $Cu_xTi_yO_z$ library. Measurements were collected on samples in the inkjet printed Y-La-Cu-Ti library on a 2 mm × 2 mm grid whereas the sputtered $Cu_xTi_yO_z$ gradient library was evaluated on a 4 mm × 8 mm grid.

The photocurrent at different potentials was extracted from the raw toggled illumination CV data by first fitting a sigmoidal function to the illuminated and dark data. In order to avoid the influence of current transients generated by illumination toggling, only the final 0.25 s of current from each 0.5 s illuminated and 0.5 s non-illuminated period were used for analysis. The net photocurrent at each potential was obtained by subtracting the fitted dark current curve from the fitted illuminated current curve.

Conventional PEC Measurement: Conventional PEC measurements were performed with a Biologic SP-200 potentiostat using a three-electrode configuration with a Pt counter electrode and 3 M Ag/AgCl reference electrode at a scan rate of 20 mV s^{-1}. The electrolyte was 0.1 M potassium bicarbonate (Sigma Aldrich, ≥99.95%) with 0.1 M sodium persulfate (Sigma Aldrich, Reagent, ≥98%) as electron scavenger at pH 8.4. A high-power light-emitting diode (340 nm, LCS-0365-48-22, Mightex) with light density of 88 mW cm^{-2} (2.45 suns equivalent) was used as the light source. All potentials reported herein were converted to reversible hydrogen electrode (RHE) scale using Equation (4).

$$E_{RHE} = E_{Ag/AgCl} + 0.21\,V + (0.059 \times pH) \tag{4}$$

The incident photon-to-current efficiency (IPCE) was measured in the same electrolyte but at a different external bias. A 150 W Xe lamp (M6255, Newport) combined with a holographic grating monochromator (CS-130, Oriel Instruments), as well as a broadband continuous light bias supplied by a high-power light-emitting diode (GCS-6500-15-A0510, Mightex), was used to illuminate the front-side of the CBO sample in a PEC cell. The differences in photocurrent and dark current responses at individual wavelengths were acquired by a Gamry Reference 600 potentiostat. The reference incident spectrum was measured by recording the photocurrent response from a calibrated Si photodiode at 5 nm intervals from 280 to 650 nm.

The absorbed photon-to-current efficiency (APCE) values were calculated by dividing IPCE by the absorbance of the CBO film, which was measured with a UV–vis spectrometer (SolidSpec3700, Shimadzu), according to Equation (5).

$$APCE(\lambda) = IPCE(\lambda) / \left[1 - T(\lambda) - R(\lambda)\right] \tag{5}$$

Transient open circuit potential was measured by a home-built system. Potential difference was recorded by the same Biologic SP-200 potentiostat. The working electrode was exposed to a white LED (MCWHL2, Thorlabs) with power of 20 mW. A blue LED (M340L4, Thorlabs) with variable power density was used as the modulating light

source, alternating between 200 ms on time and 800 ms off time. The electrolyte was 0.1 M potassium bicarbonate.

Supporting Information

Supporting Information is available from the Wiley Online Library or from the author.

Acknowledgements

Z.Z. and S.A.L. contributed equally to this work. This material was based upon work performed by the Joint Center for Artificial Photosynthesis, a DOE Energy Innovation Hub, supported through the Office of Science of U.S. Department of Energy under Award Number DE-SC0004993. EDX mapping was performed at the Molecular Foundry, supported by the Office of Science, Office of Basic Energy Science, of the U.S. Department of Energy under Contract No. DE-AC02-05CH11231. Z.Z. also acknowledges the Chinese scholarship council (CSC) for providing funding.

Conflict of Interest

The authors declare no conflict of interest.

Keywords

fermi level engineering, high-throughput methodology, passivation layer, p-type semiconductor, solar photochemistry

[1] a) F. F. Abdi, S. P. Berglund, *J. Phys. D: Appl. Phys.* **2017**, *50*, 193002; b) I. Sullivan, B. Zoellner, P. A. Maggard, *Chem. Mater.* **2016**, *28*, 5999.

[2] a) D. Cao, N. Nasori, Z. Wang, Y. Mi, L. Wen, Y. Yang, S. Qu, Z. Wang, Y. Lei, *J. Mater. Chem. A* **2016**, *4*, 8995; b) D. Kang, J. C. Hill, Y. Park, K.-S. Choi, *Chem. Mater.* **2016**, *28*, 4331; c) G. Sharma, Z. Zhao, P. Sarker, B. A. Nail, J. Wang, M. N. Huda, F. E. Osterloh, *J. Mater. Chem. A* **2016**, *4*, 2936; d) F. Wang, A. Chemseddine, F. F. Abdi, R. van de Krol, S. P. Berglund, *J. Mater. Chem. A* **2017**, *5*, 12838; e) F. Wang, W. Septina, A. Chemseddine, F. F. Abdi, D. Friedrich, P. Bogdanoff, R. van de Krol, S. D. Tilley, S. P. Berglund, *J. Am. Chem. Soc.* **2017**, *139*, 15094; f) S. P. Berglund, F. F. Abdi, P. Bogdanoff, A. Chemseddine, D. Friedrich, R. van de Krol, *Chem. Mater.* **2016**, *28*, 4231.

[3] G. Segev, C.-M. Jiang, J. K. Cooper, J. Eichhorn, F. M. Toma, I. D. Sharp, *Energy Environ. Sci.* **2018**, *11*, 904.

[4] a) J. W. Jang, D. Friedrich, S. Müller, M. Lamers, H. Hempel, S. Lardhi, Z. Cao, M. Harb, L. Cavallo, R. Heller, R. Eichberger, R. van de Krol, F. F. Abdi, *Adv. Energy Mater.* **2017**, *7*, 1701536; b) C. Zachaus, F. F. Abdi, L. M. Peter, R. van de Krol, *Chem. Sci.* **2017**, *8*, 3712; c) J. K. Cooper, S. B. Scott, Y. Ling, J. Yang, S. Hao, Y. Li, F. M. Toma, M. Stutzmann, K. V. Lakshmi, I. D. Sharp, *Chem. Mater.* **2016**, *28*, 5761; d) G. Wang, Y. Ling, X. Lu, F. Qian, Y. Tong, J. Z. Zhang, V. Lordi, C. Rocha Leao, Y. Li, *J. Phys. Chem. C* **2013**, *117*, 10957; e) P. Newhouse, D. Guevarra, M. Umehara, D. Boyd, L. Zhou, J. Cooper, J. Haber, J. Gregoire, *Chem. Commun.* **2019**, *55*, 489; f) I. S. Cho, M. Logar, C. H. Lee, L. Cai, F. B. Prinz, X. Zheng, *Nano Lett.* **2014**, *14*, 24.

[5] a) Z. Zhang, S. A. Lindley, R. Dhall, K. Bustillo, W. Han, E. Xie, J. K. Cooper, *ACS Appl. Energy Mater.* **2019**, *2*, 4111; b) I. Sullivan, P. P. Sahoo, L. Fuoco, A. S. Hewitt, S. Stuart, D. Dougherty, P. A. Maggard, *Chem. Mater.* **2014**, *26*, 6711.

[6] R. Liu, Z. Zheng, J. Spurgeon, X. Yang, *Energy Environ. Sci.* **2014**, *7*, 2504.

[7] T. Hisatomi, F. Le Formal, M. Cornuz, J. Brillet, N. Tétreault, K. Sivula, M. Grätzel, *Energy Environ. Sci.* **2011**, *4*, 2512.

[8] a) C. Battaglia, X. Yin, M. Zheng, I. D. Sharp, T. Chen, S. McDonnell, A. Azcatl, C. Carraro, B. Ma, R. Maboudian, R. M. Wallace, A. Javey, *Nano Lett.* **2014**, *14*, 967; b) Y. W. Chen, J. D. Prange, S. Dühnen, Y. Park, M. Gunji, C. E. D. Chidsey, P. C. McIntyre, *Nat. Mater.* **2011**, *10*, 539; c) P. Nunez, M. H. Richter, B. D. Piercy, C. W. Roske, M. Cabán-Acevedo, M. D. Losego, S. J. Konezny, D. J. Fermin, S. Hu, B. S. Brunschwig, N. S. Lewis, *J. Phys. Chem. C* **2019**, *123*, 20116; d) C. Du, M. Zhang, J.-W. Jang, Y. Liu, G.-Y. Liu, D. Wang, *J. Phys. Chem. C* **2014**, *118*, 17054; e) O. Zandi, T. W. Hamann, *J. Phys. Chem. Lett.* **2014**, *5*, 1522.

[9] C. Jiang, R. Wang, B. A. Parkinson, *ACS Comb. Sci.* **2013**, *15*, 639.

[10] Y. Lin, R. Kapadia, J. Yang, M. Zheng, K. Chen, M. Hettick, X. Yin, C. Battaglia, I. D. Sharp, J. W. Ager, A. Javey, *J. Phys. Chem. C* **2015**, *119*, 2308.

[11] L. Pan, J. H. Kim, M. T. Mayer, M.-K. Son, A. Ummadisingu, J. S. Lee, A. Hagfeldt, J. Luo, M. Grätzel, *Nat. Catal.* **2018**, *1*, 412.

[12] a) J. M. Gregoire, C. Xiang, X. Liu, M. Marcin, J. Jin, *Rev. Sci. Instrum.* **2013**, *84*, 024102; b) M. L. Green, I. Takeuchi, J. R. Hattrick-Simpers, *J. Appl. Phys.* **2013**, *113*, 231101; c) T. H. Muster, A. Trinchi, T. A. Markley, D. Lau, P. Martin, A. Bradbury, A. Bendavid, S. Dligatch, *Electrochim. Acta* **2011**, *56*, 9679; d) R. A. Potyrailo, K. Rajan, K. Stoewe, I. Takeuchi, B. Chisholm, H. Lam, *ACS Comb. Sci.* **2011**, *13*, 579.

[13] S. P. Berglund, H. C. Lee, P. D. Nunez, A. J. Bard, C. B. Mullins, *Phys. Chem. Chem. Phys.* **2013**, *15*, 4554.

[14] D. Guevarra, A. Shinde, S. K. Suram, I. D. Sharp, F. M. Toma, J. A. Haber, J. M. Gregoire, *Energy Environ. Sci.* **2016**, *9*, 565.

[15] F. X. Zhang, S. K. Saxena, *Appl. Phys. Lett.* **2006**, *88*, 141926.

[16] a) F. Le Formal, K. Sivula, M. Grätzel, *J. Phys. Chem. C* **2012**, *116*, 26707; b) Q. Shi, S. Murcia-López, P. Tang, C. Flox, J. R. Morante, Z. Bian, H. Wang, T. Andreu, *ACS Catal.* **2018**, *8*, 3331.

[17] a) X. Yang, R. Liu, C. Du, P. Dai, Z. Zheng, D. Wang, *ACS Appl. Mater. Interfaces* **2014**, *6*, 12005; b) S. Liu, Z. Luo, L. Li, H. Li, M. Chen, T. Wang, J. Gong, *Nano Energy* **2018**, *53*, 125.

[18] a) I. Ganesh, P. P. Kumar, I. Annapoorna, J. M. Sumliner, M. Ramakrishna, N. Y. Hebalkar, G. Padmanabham, G. Sundararajan, *Appl. Surf. Sci.* **2014**, *293*, 229; b) A. Borodin, M. Reichling, *Phys. Chem. Chem. Phys.* **2011**, *13*, 15442; c) G. X. R. Smith, R. Crook, J. D. Wadhawan, *J. Phys.: Conf. Ser.* **2013**, *471*, 012045; d) S. Vyas, R. Tiwary, K. Shubham, P. Chakrabarti, *Superlattices Microstruct.* **2015**, *80*, 215.

[19] Z. Chen, T. F. Jaramillo, T. G. Deutsch, A. Kleiman-Shwarsctein, A. J. Forman, N. Gaillard, R. Garland, K. Takanabe, C. Heske, M. Sunkara, E. W. McFarland, K. Domen, E. L. Miller, J. A. Turner, H. N. Dinh, *J. Mater. Res.* **2010**, *25*, 3.

[20] T. Hisatomi, H. Dotan, M. Stefik, K. Sivula, A. Rothschild, M. Gratzel, N. Mathews, *Adv. Mater.* **2012**, *24*, 2699.

[21] X. Yang, C. Du, R. Liu, J. Xie, D. Wang, *J. Catal.* **2013**, *304*, 86.

[22] J. Bisquert, P. Cendula, L. Bertoluzzi, S. Gimenez, *J. Phys. Chem. Lett.* **2014**, *5*, 205.

[23] F. H. Pollak, H. Shen, *Mater. Sci. Eng.: R: Rep.* **1993**, *10*, xv.
[24] a) M. Schultze, K. Ramasesha, C. D. Pemmaraju, S. A. Sato, D. Whitmore, A. Gandman, J. S. Prell, L. J. Borja, D. Prendergast, K. Yabana, D. M. Neumark, S. R. Leone, *Science* **2014**, *346*, 1348; b) S. R. Pendlebury, M. Barroso, A. J. Cowan, K. Sivula, J. Tang, M. Grätzel, D. Klug, J. R. Durrant, *Chem. Commun.* **2011**, *47*, 716.
[25] J. K. Cooper, S. E. Reyes-Lillo, L. Hess, C.-M. Jiang, J. B. Neaton, I. D. Sharp, *J. Phys. Chem. C* **2018**, *122*, 20642.
[26] E. A. Kraut, R. W. Grant, J. R. Waldrop, S. P. Kowalczyk, *Phys. Rev. B* **1983**, *28*, 1965.
[27] R. Marschall, *Adv. Funct. Mater.* **2014**, *24*, 2421.
[28] J. A. Haber, Y. Cai, S. Jung, C. Xiang, S. Mitrovic, J. Jin, A. T. Bell, J. M. Gregoire, *Energy Environ. Sci.* **2014**, *7*, 682.